Macromolecules **2007,** *40,* 4691−4702

Semi-Grand Canonical Monte Carlo (SGMC) Simulations to Interpret Experimental Data on Processed Polymer Melts and Glasses

Frederick E. Bernardin, III and Gregory C. Rutledge*

Department of Chemical Engineering, Massachusetts Institute of Technology, Cambridge, Massachusetts 02139

Received December 21, 2006; Revised Manuscript Received March 1, 2007

ABSTRACT: We describe the application of the semi-grand canonical Monte Carlo (SGMC) method to analyze and interpret experimental data for nonequilibrium polymer melts and glasses. Experiments that provide information about atomic-level ordering, e.g., birefringence, are amenable to this approach. Closure of the inverse problem of determining the structural detail from limited data is achieved by selecting the lowest-free-energy ensemble of configurations that reproduces the experimental data. The free energy is calculated using the thermodynamic potential of the appropriate semi-grand canonical (SGC) ensemble [$NPT\Delta\mu(\boldsymbol{I})$], as defined by the experimental data. To illustrate the method, we examine uniaxially oriented polyethylene melts of average chain length up to C_{400}. The simulation results are analyzed for features not explicitly measured by birefringence, such as the density, torsion angle distribution, molecular scale orientation, and free energy, to understand more fully the underlying features of these nonequilibrium states. The stress-optical rule for polyethylene is evaluated in this way.

1. Introduction

One of the hallmarks of polymers is the ease with which they can be processed into anisotropic materials. The persistence of these anisotropic states, despite their inherently nonequilibrium nature, is the key to the versatile optical and mechanical properties of polymers. Deducing the microstructure of these anisotropic states from their observed properties is, by its very nature, an inverse problem; the enormous number of structural degrees of freedom at the atomic scale ensures that even the most sophisticated battery of measurements will leave the structure severely underdetermined. Statistical mechanics provides various tools whereby a representative sample of these degrees of freedom can be averaged to calculate a corresponding measurable macroscopic property. Semi-grand canonical Monte Carlo (SGMC) is one such tool that allows the simulation of anisotropy in an otherwise homogeneous system by identifying each structural unit by one or more of its measurable anisotropic features. We can thus speak of a set of “physical isomers” or “physical species” that differ from each other only in their orientation. The systems are distinguished by the orientation distribution function (ODF) of these species.

Experimental data are incorporated into the SGMC simulation through the normalization of an experimental observable to match the concentration of a corresponding physical species.[1] For the uniaxially oriented systems studied here, the physical species are structural units that are distinguished according to the angle θ they form with the axis of orientation. For example, birefringence depends on the second Legendre coefficient $P_2(\cos\theta)$ of the polarizable structural units. Similarly, infrared dichroism depends on $P_2(\cos\theta)$ of the dipole of an IR-active structural unit of the molecule. Raman depolarization ratios depend on the values of both $P_2(\cos\theta)$ and the fourth Legendre coefficient $P_4(\cos\theta)$ of the relevant scattering unit. Multidimensional NMR can, in principle, provide data for the entire ODF. For highly oriented samples, DECODER-NMR and several related NMR techniques[2−4] have been shown to be particularly powerful; values for Legendre coefficients up to $P_{14}(\cos\theta)$ have been reported by these methods.[5] The reader is directed to Ward[6] for more detail on the techniques and interpretation of measurements of oriented polymer systems.

From the information provided by these experimental techniques, one can attempt to reconstruct the full ODFs, for example, through the use of maximum entropy (ME) methods[7] or reverse Monte Carlo (RMC).[8] Maximum entropy methods produce a unique and unbiased distribution function for a set of experimental constraints. However, these methods ignore important energetic interactions within the system, possibly resulting in an unphysical solution. RMC, on the other hand, can account for the chemical interactions among sites in the system but equates measurement uncertainty with thermal fluctuations in the system in a manner inconsistent with thermodynamics. Obviously, as experimental measurement techniques improve, the thermodynamics of the system should be unaffected.

SGMC is distinguished from other inverse methods by its consideration of the specific chemical and thermodynamic features of a system that may be out of equilibrium. The result is a simulation incorporating all available information about the system in a thermodynamically consistent manner. Thus, we obtain not only a more reliable estimate of the incomplete features of the orientation distribution but also a basis for estimating the other nonequilibrium characteristics of the system. We can obtain estimates of torsion angle distributions, changes in free energy, orientation on different length scales, density, and other measures that are not accessible using either experimental measurements or ME and RMC methods. It is this wealth of microscopic-level information that justifies the more intense computational expense of an SGMC simulation. We demonstrate this method for a variety of systems that span the range of orientation observed in experimental polyethylene melt studies[9−11] as well as higher orientations that have been simulated for polyethylene melts by molecular dynamics.[12,13]

2. Theory

Semi-Grand Canonical (SGC) Ensemble. The SGC ensemble is obtained by the identification of each of the N sites

---

* Corresponding author. E-mail: rutledge@mit.edu.

10.1021/ma062935r CCC: $37.00

in a system with one of several species types, indicated by a component or speciation matrix, $\mathbf{I}$; $\mathbf{I}_i$ is a vector component of $\mathbf{I}$ that designates the specific species type of site i.[14] Rewriting eqs 41 and 48 of Briano and Glandt[14] to express the SGC partition function Υ and the probability density $p(\mathbf{I})$ of the species in terms of the conjugate potential function $\mu(\mathbf{I}_i)$, we obtain the equations that provide the basis for the SGMC method:

$$\Upsilon = \frac{\exp(-\beta N\mu_r)}{N!}\int_{\mathbf{I}_1}\cdots\int_{\mathbf{I}_N} q^N Z_N \exp\Big(\beta\sum_{i=1}^{N}\mu(\mathbf{I}_i)\Big)\prod_{i=1}^{N}\mathrm{d}\mathbf{I}_i \tag{1}$$

$$p(\mathbf{I}) = \frac{1}{\Upsilon}\frac{q^N}{N!}\int_{\mathbf{I}_2}\cdots\int_{\mathbf{I}_N} Z_N \exp\Big(\beta\sum_{i=1}^{N}(\mu(\mathbf{I}_i)-\mu_r)\Big)\prod_{i=2}^{N}\mathrm{d}\mathbf{I}_i \tag{2}$$

where $Z_N = \int \exp(-\beta U(\mathbf{r}^N))\,\mathrm{d}r^N$ is the canonical configuration integral, q is a scaled internal partition function (assumed to be constant, for the purposes of this work), and μ_r is a reference potential whose value is constrained by fixing the system size to be N.

This speciation yields the nonequilibrium SGC $[NVT\Delta\mu(\mathbf{I})]$ ensemble (where $\Delta\mu(\mathbf{I}) = \mu(\mathbf{I}) - \mu_r$) by transformation of the canonical $[NVT]$ ensemble (or analogously $[NPT\Delta\mu(\mathbf{I})]$ from $[NPT]$). In the $[NVT\Delta\mu(\mathbf{I})]$ ensemble, the probability density and importance criterion necessary to satisfy the detailed balance condition follow directly from eq 2:

$$\ln p(\mathbf{r}^N,\mathbf{I}) \propto -\beta\Big[U(\mathbf{r}^N) - \sum_{i=1}^{N}\Delta\mu(\mathbf{I}_i)\Big] \tag{3}$$

$$p_{\mathrm{acc}} = \min\Big\{1, \exp\Big(-\beta\Big[U(\mathbf{r}^N)_{\mathrm{new}} - U(\mathrm{r}^N)_{\mathrm{old}} - \sum_{i=1}^{N}(\mu(\mathbf{I}_i)_{\mathrm{new}} - \mu(\mathbf{I}_i)_{\mathrm{old}})\Big]\Big)\Big\} \tag{4}$$

Methods for the iterative determination of $\mu(\mathbf{I})$ to reproduce the desired $p(\mathbf{r}^N,\mathbf{I})$ have been reported elsewhere.[1,15,16] The value of μ_r may be determined a posteriori by methods such as thermodynamic integration or the self-consistent histogram method.[17] In general, it is unnecessary to evaluate μ_r because it is a constant and does not affect the distributions.

A system that is physically inhomogeneous, yet chemically homogeneous, can be simulated in the SGC ensemble by choosing a physical, rather than chemical, variable to identify each site. This was originally demonstrated for a Lennard-Jones (LJ) fluid by identifying each site by the $(N - 1)$ pairwise intermolecular distances the site forms with the other sites in the system, i.e., its contribution to the radial distribution function (RDF); the conjugate potential determined by iteration in this case is just the conventional two-body interaction potential.[1] The same identification was subsequently evaluated for intra- as well as intermolecular interaction potentials using the Gō model[18] for proteins as a test case.[14] Procedurally similar methods to determine interaction potentials have been proposed and justified on different grounds by Soper,[19] Lyubartsev et al.,[20] Müller-Plathe,[21] and most recently, Jain et al.[22] However, the process of speciation to construct a simulation in the SGC ensemble is more general. It can solve not only for the potentials intrinsic to materials but also for potentials or fields that perturb the system out of equilibrium. Colhoun et al., originally employed this capability to follow the relaxation of polystyrene molecular conformations after shearing.[23] In that work, the use of the SMAS-DECODER NMR method allowed the determination of the full ODF prior to its use in a SGMC simulation. In this work, we consider the use of SGMC to study systems given only incomplete information about the ODF, as is more commonly the case from birefringence and the other measurement methods mentioned earlier.

The motivation for using a Monte Carlo method to study nonequilibrium states is that the method samples the optimal ensemble of configurations that reproduces the available observations (i.e., the experimental measurements). Relative to molecular dynamics, the Monte Carlo method permits the introduction of nonphysical moves that sample phase space more efficiently. The structures produced by a nonequilibrium molecular dynamics simulation (NEMD) may be sensitive to the rate of deformation employed in the simulation, which typically exceeds by several orders of magnitude those available experimentally. In contrast, the SGMC method constructs a molecular model that reproduces the available experimental data assuming only the applicability of the force field. The result is a quasi-equilibrium state that can be identified closely with a perturbation on the time scale of the delay between experimental measurements.

Ultimately, the goal of modeling is to anticipate behavior that is not obvious from the experimental measurement. A real strength of molecular modeling is the ability to query the simulated ensemble and quantify characteristics of the most probable ensemble of molecular configurations. These characteristics, which may not be accessible by conventional analytical techniques, provide a window into the structural changes taking place in the polymer melt. This is not to say that the extracted characteristics of the system are the true ones, but rather that they are the most probable ones given the limited information available. The method also allows the evaluation of complementary sets of experimental data, either individually or jointly, to determine whether they are consistent and nondegenerate in the information they provide about the state of the system.

Maximum Entropy: The Moments Problem. Nearly a half-century ago, Jaynes showed the equivalence of the maximum entropy (ME) estimates of information theory and the ensembles obtained from statistical mechanics.[24] The ME estimate involves an iterative calculation of a potential conjugate to each of the independent constraints using the method of Lagrange multipliers.[25] These constraints are the measured (or known) values of the system, which are then "simulated" in an ensemble that holds their conjugate potentials constant. Therefore, the adaptation of this approach is not simply a mathematical convenience. Our statistical approach to modeling ensembles makes this evaluation of a potential *identical* to the statistical mechanical description of the most likely nonequilibrium ensemble that is consistent with our knowledge of the system.

The application of this method to determine a full distribution of any characteristic from a finite number of its moments is known as the "moments problem".[26] This is relevant to the measurement of the second moment of an orientation distribution, e.g., through birefringence, to obtain an estimate of the properties of the system. The SGMC method provides a means for adapting ME methods to complex interacting systems. In its simplest form, an ensemble with $U(\mathbf{r}^N) \equiv 0$, the SGMC method becomes identical to the ME method. The Lagrange multipliers are analogous to $\Delta\mu(\mathbf{I})$ in eq 3 (e.g., μ_k, $k = 0$ to K, see eq 5 below) and maximize the entropy S subject to the constraint that the known values of the K moments match their ensemble averages $\langle h_k(\mathbf{I})\rangle$.

In general, the SGMC potential function $\mu(\mathbf{I})$ can be written as the summation of a set of basis functions:

$$\mu(\mathbf{I}) = \sum_{k=0}^{K} \mu_k h_k(\mathbf{I}) = \mu_0 + \sum_{k=1}^{K} \mu_k h_k(\mathbf{I}) \tag{5}$$

The moments $\langle h_k \rangle$ and the change in entropy ΔS with respect to the condition $\mu(\mathbf{I}) = 0$ for a noninteracting system are then found to be:[24]

$$\langle h_k(\mathbf{I})\rangle = \int h_k(\mathbf{I}) p(\mathbf{I})\, \mathrm{d}\mathbf{I} = \int h_k(\mathbf{I}) \exp\{\beta \sum_{k=0}^{K} \mu_k h_k(\mathbf{I})\}\, \mathrm{d}\mathbf{I} \tag{6}$$

$$\frac{\Delta S}{k_\mathrm{B}} = -\int p(\mathbf{I}) \ln p(\mathbf{I})\, \mathrm{d}\mathbf{I} = -\beta \sum_{k=0}^{K} \mu_k \langle h_k(\mathbf{I})\rangle \tag{7}$$

where μ_0 is chosen such that $p(\mathbf{I})$ is normalized. The convexity of the functional form of eq 7 ensures a unique solution for $\mu(\mathbf{I})$, if one exists.[27] This uniqueness can be extended to interacting systems by recognizing that weighting states (e.g., by their interaction energies) does not affect the existence of a unique solution.[28] This property guarantees the closure of the inverse problem being solved here by SGMC.

One potential difficulty with reconstructing a detailed atomistic system from a limited set of measured moments is that the Lagrange multipliers may oscillate and not converge as the size of the basis set K increases for a nonorthogonal basis set.[29] This problem is resolved through orthonormalization of the basis sets as discussed below. With both SGMC and ME methods, the nature of the experimental data will guide the choice of the basis functions as well as the number of terms used in the basis set K to provide a best solution to the inverse problem of estimating the complete distribution.

Molecular Representation. The selection of physical isomers is motivated by the experimental measurement of the physical organization of the molecules. Significantly, for most of the experimental methods mentioned in the Introduction, these physical isomers will be local in nature, involving only one or a few bonds.

For a polymeric system comprised of N atoms or sites, distributed among N_ch chains, the Cartesian coordinate of the ith site of the jth chain can be written $\mathbf{r}_{i,j}$. The intramolecular coordinates are equivalently represented in terms of connector vectors $\mathbf{q}_{i,j}^{(m)}$ of the n_j sites in each chain. The superscript m indicates the number of bonds spanned by the connector. Connector vectors that coincide with the backbone bonds are represented as:

$$\mathbf{q}_{i,j}^{(1)} = \mathbf{r}_{i+1,j} - \mathbf{r}_{i,j}; \qquad i = 1, 2, ..., n_j - 1 \tag{8}$$

Other connector vectors can be similarly defined; for example, next-nearest-neighbor sites in polyethylene, which provide an estimate of the local chain direction, are represented:

$$\mathbf{q}_{i,j}^{(2)} = \mathbf{r}_{i+2,j} - \mathbf{r}_{i,j}; \qquad i = 1, 2, ..., n_j - 2 \tag{9}$$

and the end-to-end vector $\mathbf{Q}_j$ of chain j is defined as:

$$\mathbf{Q}_j = \mathbf{q}_j^{(n_j-1)} = \mathbf{r}_{n_j,j} - \mathbf{r}_{1,j} \tag{10}$$

For molecules with rigid intramolecular bonds and bond angles, $\mathbf{q}_{i,j}^{(1)}$ and $\mathbf{q}_{i,j}^{(2)}$ are fixed in magnitude, and they can be described unambiguously by their corresponding unit vectors $\mathbf{e}_{i,j}^{(1)}$ and $\mathbf{e}_{i,j}^{(2)}$:

$$\mathbf{e}_{i,j}^{(1)} = \frac{\mathbf{q}_{i,j}^{(1)}}{|\mathbf{q}_{i,j}^{(1)}|} \tag{11a}$$

$$\mathbf{e}_{i,j}^{(2)} = \frac{\mathbf{q}_{i,j}^{(2)}}{|\mathbf{q}_{i,j}^{(2)}|} \tag{11b}$$

However, the magnitude of $\mathbf{Q}_j$ will not, in general, be fixed, necessitating both an orientation (unit vector) and scalar magnitude to characterize its distribution.

Application of the SGMC method requires the conservation of the total number of speciated elements. For a monodisperse polymer system, n_j is constant and the number of connector vectors is strictly conserved and equal for each molecule. In general, we use variable-connectivity moves to simulate polymer systems, in which N and N_ch are fixed but $\{n_j\}$ are not. For such systems, the number of connector vectors is not conserved for $\mathbf{q}_{i,j}^{(m)}$ if $m > n_\mathrm{min}$, the shortest chain in the simulation, violating this fundamental requirement of the SGMC method. However, for all cases considered here, the size of the structural units is smaller than n_min and so is always conserved. For fixed N_ch, the number of end-to-end connectors is conserved by construction, making the set $\{\mathbf{Q}_\mathrm{j}\}$ a viable physical isomer in the SGC ensemble, despite m being larger than n_min.

Selection of Basis Set. In general, eq 3 can be written as:

$$\ln p(\mathbf{r}^N, \mathbf{I}) \propto -\beta[U(\mathbf{r}^N) - \sum_{i=1}^{N} \sum_{k=0}^{K} \mu_k h_k(\mathbf{I}_i)] \tag{12}$$

where now $h(\mathbf{I})$ represents a generalized basis function. Colhoun et al.[23] provided a demonstration of the SGMC method for molecular orientation, effectively using a boxcar function for the multidimensional speciation of a polymer system based on the polar angles of $\mathbf{e}_{i,j}^{(2)}$, $I \equiv \{\cos \theta^{(2)}, \phi^{(2)}\}$, where $\cos \theta^{(2)} = \mathbf{e}_{i,j}^{(2)} \cdot \mathbf{e}_x$ and $\tan \phi^{(2)} = (\mathbf{e}_{i,j}^{(2)} \cdot \mathbf{e}_y)/(\mathbf{e}_{i,j}^{(2)} \cdot \mathbf{e}_z)$. The corresponding uniaxial form $I \equiv \{\cos \theta^{(2)}\}$ of this basis set is:

$$\begin{aligned} p(\cos \theta^{(2)}) &= \sum_{k=1}^{K} h_k(\mathbf{I}_i) \\ &= \sum_{k=1}^{K} c_k[H(\cos \theta^{(2)} - \cos \theta_{k-}^{(2)}) - \\ &\qquad H(\cos \theta^{(2)} - \cos \theta_{k+}^{(2)})] \end{aligned} \tag{13}$$

where $H(x)$ is the Heaviside function and $\cos \theta_{k+}^{(2)}$ and $\cos \theta_{k-}^{(2)}$ are the upper and lower limits of the kth bin. The resolution of the histogram is limited only by the numerical precision or the ability to populate each bin statistically during a single simulation.

As the number of bins becomes large, it is often more practical to represent $p(\cos \theta^{(m)})$ as a series of continuous basis functions. For $\mathbf{e}_{i,j}^{(1)}$ or $\mathbf{e}_{i,j}^{(2)}$, a particularly relevant form is the polynomial expansion for the ODF using basis functions of the form $h_k(\mathbf{e}^{(2)}) \equiv (\mathbf{e}^{(2)t}\cdot)^k/k!$, where the superscript t denotes the transpose. For cases involving connector vectors described in this work, the ODF generally exhibits mirror symmetry, and odd-order terms in $\mathbf{e}_i^{(m)}$ average to zero. The ODF then becomes:

$$\ln p(\mathbf{e}^{(2)}) = A_0^{(2)} + \frac{1}{2}\,\mathbf{e}^{(2)t}\cdot\mathbf{A}_2^{(2)}\cdot\mathbf{e}^{(2)} + ... = \sum_{k=0}^{K/2} \frac{(\mathbf{e}^{(2)t}\cdot)^{2k}}{(2k)!}\,\mathbf{A}_{2k}^{(2)} \tag{14}$$

We can obtain a polynomial expansion over the interval [−1,1] in x, y, and z by expanding eq 14:

$$\ln p(\mathbf{e}^{(2)}) = A_0^{(2)} + \sum_{j=x,y,z} A_{2,j}^{(2)} \cos^2 \theta_j^{(2)} + ... \tag{15}$$

which produces a distribution by specifying $\{\langle\cos^{2k}\theta_j^{(2)}\rangle\}$ and determining the conjugates $\{A_{2k,j}^{(2)}\}$, for $j = x, y, z$, as in the moments problem discussed above. Upon application of the Gram−Schmidt orthonormalization, one obtains the Legendre polynomial expansion:

$$\ln p(\mathbf{e}^{(2)}) = A_0'^{(2)} + \sum_{j=x,y,z} A_{2,j}'^{(2)} P_2(\cos\theta_j^{(2)}) + ... \tag{16}$$

This form suggests a new set of species types or physical isomers that are defined by the polynomials, $P_{2k}(\cos\theta^{(2)})$. These are linearly related to the original isomers defined by $\cos^{2k}\theta^{(2)}$ and provide an equivalent expression for $\ln p(\mathbf{e}^{(2)})$. The leading term $A_0'^{(2)}$ is constant and may be dropped. Equation 12 then takes the specific form:

$$\ln p(r^N,\{P_{2k}^N\}) \propto -\beta[U(\mathbf{r}^N) - \sum_{i=1}^{N}\sum_{k=1}^{K/2}\sum_{j=x,y,z} \mu_{2k,j}^{(2)} P_{2k}(\cos\theta_{i,j}^{(2)})] \tag{17}$$

where $\mu_{2k,j}^{(2)}$ can be directly identified as $A_{k,j}'^{(2)}/\beta$ in eq 16. Because $P_2(\cos\theta_x^{(2)})$ is typically proportional to the birefringence, eq 17 can be truncated after $k = 1$ and $\mu_{2k,y}^{(2)} = \mu_{2k,z}^{(2)} = 0$ to obtain an appropriate form for use with these measurements. Similarly, other measures of uniaxial orientation will be truncated after $k = 1$ (infrared), $k = 2$ (Raman), or some $k > 2$ (NMR).

Relation to Melt Elasticity. While we have been motivated by the nature of experimental measurements to simulate orientation in polymers using a local orientation potential, Mavrantzas and co-workers were motivated by studies of melt elasticity in elongational flows and proposed a new free energy function for a flow-oriented polymer melt in terms of new, molecular structural variables. This resulted in a similar description of nonequilibrium polymer systems in terms of the conformation tensor[30−32] or, alternatively, in terms of the normal modes.[33] They defined the conformation tensor for chain j, $\mathbf{c}_j$, as:

$$\mathbf{c}_j = \frac{3\mathbf{Q}_j\mathbf{Q}_j}{\langle Q_j^2\rangle_0} \tag{18}$$

where $\langle Q_j^2\rangle_0$ is the mean squared end-to-end distance of the jth chain in the unperturbed state. The selection of $\mathbf{c}_j$ as the structural parameter to describe the nonequilibrium state space was inspired by its prevalence in rheological models of polymer systems and by the intuition that it accurately represents the "slowest" degrees of freedom, those most likely to deviate from their equilibrium values under conditions of flow. The probability distribution can then be written, to within an additive constant, as:

$$\ln p(\mathbf{Q}_j) = \alpha{:}\mathbf{c}_j \tag{19}$$

where α is a new thermodynamic potential conjugate to $\mathbf{c}_j$.

Despite their differences in origin and motivation, we believe that there exists an intimate connection between the approach of Mavrantzas and co-workers and the SGMC ensemble approach elaborated here. Comparing the two approaches can offer some insight into both methods. To show this, we start with eq 14, substitute $\mathbf{Q}_j/Q_j$ for $\mathbf{e}^{(2)}$, invoke mirror symmetry as before and truncate the expansion at the second moment term. Doing so, we obtain:

$$\ln p(\mathbf{Q}_j) = \frac{1}{2}\frac{(\mathbf{Q}_j)^t\cdot\mathbf{A}_2\cdot\mathbf{Q}_j}{Q_j^2} = \frac{1}{2}\frac{\mathbf{A}_2{:}\mathbf{Q}_j\mathbf{Q}_j}{Q_j^2} \tag{20}$$

We next define two new variables, Λ_j^2 and $\mathbf{S}_j$, to represent the size and orientation, respectively, of the conformation tensor of chain j with respect to its undeformed state:

$$\Lambda_j^2 = \frac{tr(\mathbf{Q}_j\mathbf{Q}_j)}{\langle Q_j^2\rangle_0} \tag{21a}$$

$$\mathbf{S}_j = (3\mathbf{e}_j^{(Q)}\mathbf{e}_j^{(Q)} - \mathbf{I})/2 \tag{21b}$$

Here, $\mathbf{I}$ is the 3 × 3 identity tensor. The diagonal elements of $\mathbf{S}_j$ are the second Legendre polynomials of the vector $\mathbf{Q}_j$ with respect to the three Cartesian axes, and $\mathbf{S}_j$ is traceless. Using these definitions, the conformation tensor for chain j defined by eq 18 can be written as follows:

$$\mathbf{c}_j = \frac{3\mathbf{Q}_j\mathbf{Q}_j}{\langle Q_j^2\rangle_0} = \Lambda_j^2(2\mathbf{S}_j + \mathbf{I}) \tag{22}$$

while eq 20 becomes:

$$\ln p(\mathbf{Q}_j) = \frac{\mathbf{A}_2{:}\mathbf{c}_j}{6\Lambda_j^2} = \frac{1}{6}\,\mathbf{A}_2{:}(2\mathbf{S}_j + \mathbf{I}) \tag{23}$$

Comparison of eqs 19 and 23 suggests that $\mathbf{A}_2 = 6\Lambda_j^2\alpha$ and one can write:

$$\ln p(\mathbf{Q}_j) = 2\Lambda_j^2\alpha{:}\mathbf{S}_j + \Lambda_j^2 tr(\alpha) \tag{24}$$

In the SGC ensemble, $\mathbf{A}_2 = 3\beta\mu_2^{(Q)}$, where $\mu_2^{(Q)}$ has been defined as the end-to-end vector orientation potential. The tensors $\mu_2^{(Q)}$ and α can *always* be specified to obtain the equality $2\alpha = \beta\mu_2^{(Q)}$. In general, the form of α (and therefore $\beta\mu_2^{(Q)}$ in this comparison) is specified by the velocity gradient tensor for a given flow.[33] For the special case of traceless diagonal α that describes uniaxial elongational flow,[33] the melt elasticity approach can be reproduced by SGMC using:

$$\ln p(\mathbf{r}^N,\mathbf{Q}^{N_{\mathrm{ch}}}) = -\beta[U(\mathbf{r}^N) - \sum_{j=1}^{N_{\mathrm{ch}}} \Lambda_j^2(\mu_2^{(Q)}{:}\mathbf{S}_j)] \tag{25}$$

Because $\mathbf{S}$ is also traceless, it turns out that any arbitrary value can be added to the diagonal components of μ in eq 25 with no effect on the resulting distribution of $\mathbf{Q}$ produced by simulation. Therefore, as a matter of practicality in this work, the melt elasticity approach with a uniaxial traceless α was reproduced using a form of $\beta\mu$ with a single nonzero component $\beta\mu_{xx} = 3\alpha_{xx}$ ($= -6\alpha_{yy} = -6\alpha_{zz.}$) in eq 25; subtracting $\alpha_{xx}\mathbf{I}$ from this form recovers the original $\beta\mu_2^{(Q)}$ with no change on the distribution of **Q** obtained by simulation.

Instead of coupling the physical potential to the conformation tensor, it may be desirable in some circumstances to introduce a second speciation parameter for the chain size, Λ_j^2. This is consistent with rheological models such as the "pompon" model described by Öttinger[34] and employed by Mavrantzas and Öttinger,[33] in which independent variables for orientation $\mathbf{S}_j$ and stretch Λ_j^2 are defined. We introduce a second potential $\mu_2^{(\Lambda)}$ for the chain size and rewrite the orientation potential as $\mu_2^{(S)}$ to clarify its coupling to $\mathbf{S}_j$. The probability density becomes:

$$\ln p(\mathbf{r}^N,\mathbf{Q}^{N_{\mathrm{ch}}}) = -\beta[U(\mathbf{r}^N) - \sum_{j=1}^{N_{\mathrm{ch}}} (\mu_2^{(S)}:\mathbf{S}_j) - \mu_2^{(\Lambda)}\sum_{j=1}^{N_{\mathrm{ch}}} \Lambda_j^2] \tag{26}$$

Equation 26 has the form of physical isomerism defined by a two-dimensional speciation variable, $\{\mathbf{S}, \Lambda^2\}$, in which the variables are separable and independent. A similar approximation was also recognized by Mavrantzas and Theodorou.[32]

The separation of physical isomerism into two components, based on orientation (the $\mathbf{S}_j$ term) and size (the Λ_j^2 term), as shown in eq 26, reveals an interesting difference from the use of the conformation tensor; application of $\mu_2^{(S)}$ with $\mu_2^{(\Lambda)} = 0$ produces only rotational forces that do not contribute to the system pressure. In contrast, application of α (or similarly, $\mu_2^{(Q)}$) or $\mu_2^{(\Lambda)}$ results in stretching forces. These stretching forces are responsible for the pressure changes documented previously[30] and create a contribution to the pressure that is not coupled to the volume, but rather to the applied physical potential. In those simulations, the system pressure P is the trace of the sum of the volume-coupled term $b\mathbf{I}$ and the stress due to the applied physical potential $\tau^{(\mu)}$ as shown in eq 8 of ref 30. The pressure contribution of the potential is traceless only if the potential acts exclusively on the orthonormalized components of the direction of a nonrigid unit, as is the case for $\mu^{(S)}$, with no direct effect on the size. Derivation of the stresses due to orientation and their numerical validation against the simulated virial stresses are given in the Appendix.

3. Simulation Method

We use the united atom polyethylene model originally proposed by Paul et al.[35] with modifications described by Veld et al.[36] The force field contribution due to site i is:

$$\begin{aligned} E_i &= E_{b,i} + E_{\theta,i} + E_{\tau,i} + \frac{1}{2}\sum_{\substack{j=1\\ j\neq i}}^{N} \mathrm{E}_{LJ,ij} \\ &= \frac{1}{2}k_b(b_i - b_0)^2 + \frac{1}{2}\frac{k_\theta}{\sin\theta}(\cos\theta_i - \cos\theta_0)^2 + \\ &\qquad \sum_{n=1}^{3} k_{\tau,n,i}(1 - \cos n\phi) + \frac{1}{2}\sum_{\substack{j=1\\ j\neq i}}^{N} 4\epsilon\left[\left(\frac{\sigma}{r_{ij}}\right)^{12} - \left(\frac{\sigma}{r_{ij}}\right)^{6}\right] \end{aligned} \tag{27}$$

with the following parameters: $k_b = 37.61$ kJ/mol/nm^2, $b_0 = 0.153$ nm, $k_\theta = 502.1$ kJ/mol, $\theta_0 = 68.0°$, $k_{\tau,1} = 6.69$ kJ/mol, $k_{\tau,2} = 3.63$ kJ/mol, $k_{\tau,3} = 13.56$ kJ/mol, $\epsilon = 390.95$ J/mol, and $\sigma = 0.4009$ nm. The Lennard-Jones (LJ) cutoff is 2.5σ with a corresponding long-range energy correction.

During a simulation, the following Monte Carlo moves were employed: (1) site translation, (2) reptation, (3) rebridging,[37] (4) end rotation, (5) end-bridging,[38] and (6) volume change. In the site translation move, the Cartesian coordinates of a single site were changed by a random displacement within a range whose maximum was adjusted to maintain a targeted acceptance of 50%. In the reptation move, a site was removed from one end of a chain and appended to the other end of the same chain or to the end of a different chain, while keeping the bond length and angle constant; the new torsion angle was perturbed from the old one by a random value adjusted to maintain 50% acceptance. In the rebridging move, three consecutive sites were selected at random from the middle of the chain, and a nonlinear equation was solved to determine alternative configurations of these three sites that reconnect the chain sections while keeping bond lengths and angles constant; the move was selected randomly from among these alternative configurations. In the end rotation move, the torsion at a randomly selected chain end was perturbed by a random amount within a range whose maximum was adjusted to maintain the targeted acceptance of 50%. In the end-bridging move, three consecutive sites in the vicinity of a chain end were selected. A nonlinear equation was solved, as in rebridging, except that the sites were placed so as to connect part of the original chain to the end of its neighbor. In the volume change move, the edge length of the simulation cell was changed by a small random amount, within a range whose maximum was adjusted to maintain the targeted acceptance of 50%, and the chain centers-of-mass were displaced affinely. The attempt frequency and typical fraction of accepted moves (for the isotropic melt) were, respectively: site translation, 0.55 and 0.50; reptation, 0.11and 0.13; rebridging, 0.11and 0.20; end rotation, 0.11 and 0.50; end bridging, 0.11and 0.10. Volume changes were attempted, on average, once every N moves with an acceptance of 0.50.

The use of variable connectivity moves (reptation and end-bridging) means that the molecular weight of the chains is not fixed during a simulation. The resulting molecular weight (or chemical) polydispersity is controlled through the introduction of conventional residual chemical potentials μ_{MW} for chains of different molecular weight. The subscript MW is used to distinguish this chemical potential from the orientation potential introduced earlier. The following choice of μ_{MW} ensures a flat molecular weight distribution whose polydispersity index is 1.09:[39]

$$\begin{aligned} \mu_{\mathrm{MW}} &= 0, && \text{for all chains } j\ \frac{1}{2}\frac{N}{N_{\mathrm{ch}}} \leq n_j \leq \frac{3}{2}\frac{N}{N_{\mathrm{ch}}} \\ \mu_{\mathrm{MW}} &= \infty, && \text{otherwise} \end{aligned} \tag{28}$$

The parameters used for the simulations were chosen to allow comparison to previously published work[30,33,39] as well as to evaluate the effects of orientation potentials applied to different choices of connector vector in the $[NN_{\mathrm{ch}}PT\mu_{\mathrm{MW}}\Delta\mu(\mathbf{I})]$ ensemble. In each case, the simulations were run with the force field pressure contribution $P = 1$ atm, temperature $T = 450$ K, and μ_{MW} as specified by eq 28. Simulations were run for 2×10^5 to 1×10^6 MC cycles. Block averages of the orientation were used to verify the convergence of the error around the mean value obtained for the simulation. The "local" orientation potential applied to next-nearest-neighbor vectors $\mathbf{q}^{(2)}$ was of the form prescribed by eq 17 with $K = 2$ and only $\mu_{2,x}^{(2)}$ nonzero

Table 1. Values of Orientation Potential $\mu_2^{(2)}$ Used with Eq 29 (in Units of kT)

ID	N	N_{ch}	orientation potential ($\mu_2^{(2)}$/kT)
C_{24}	768	32	0, 0.025, 0.05, 0.075, 0.1, 0.15, 0.2, 0.25, 0.3, 0.35, 0.4, 0.45
C_{78}	3120	40	0, 0.025, 0.05, 0.075, 0.1, 0.15, 0.2, 0.25, 0.3
C_{156}	3120	20	0, 0.025, 0.05, 0.075, 0.1, 0.15, 0.2, 0.25
C_{400}	3200	8	0, 0.025, 0.05, 0.075, 0.1

Table 2. Values of Orientation Potential Used with Eq 31 and Eq 32 (in Units of kT)

			physical isomer potential	
MW	N_{sites}	N_{ch}	$\mu_2^{(S)}/kT$	$\mu_2^{(Q)}/kT$
C_{24}	768	32	0, 0.7, 1.0, 1.4,3.0	0, 0.9, 1.8,2.7,3.6
C_{78}	3120	40	0, 0.4, 0.8, 1.2, 1.6	0, 0.6, 1.2, 1.8, 2.4

(the subscript x on $\theta_{i,j,x}^{(2)}$ and $\mu_{2,x}^{(2)}$ is omitted henceforth for simplicity):

$$\mu = \mu_2^{(2)} \sum_{j=1}^{N_{ch}} \sum_{i=1}^{n_j} P_2(\cos \theta_{i,j}^{(2)}) \tag{29}$$

The orientation potentials employed for each of four system sizes are shown in Table 1. For each chain length, an additional simulation with three-quarters as many chains was run at the highest orientation potential to ensure that system size effects were negligible.

Two "molecular" orientation potential forms were tested by applying a potential to the vector $\mathbf{Q}_j$. Their forms were as follows:

$$\mu = \mu_2^{(S)}\colon \sum_{j=1}^{N_{ch}} \mathbf{S}_j \tag{30}$$

with all the components $\mu_{2,ij}^{(S)} = 0$ except $\mu_{2,xx}^{(S)}$. In this case, eq 30 simplifies to a form analogous to eq 29, with $\theta_{i,j}^{(2)}$ replaced by the orientation angle $\theta_j^{(Q)}$ formed by the end-to-end vector $\mathbf{Q}_j$ of chain j with respect to the orientation direction:

$$\mu = \mu_{2,xx}^{(S)} \sum_{j=1}^{N_{ch}} P_2(\cos \theta_j^{(Q)}) \tag{31}$$

Similarly, the orientation potential given by eq 25 takes the form:

$$\mu = \mu_{2,xx}^{(Q)} \sum_{j=1}^{N_{ch}} \Lambda_j^2 P_2(\cos \theta_j^{(Q)}) \tag{32}$$

Henceforth, the subscript xx on $\mu_{2,xx}^{(S)}$ and $\mu_{2,xx}^{(Q)}$ are also dropped for simplicity of notation. The orientation potentials employed with eqs 31 and 32 are shown in Table 2.

4. Results and Discussion

A. Simulations Using the Local Orientation Potential, $\mu_2^{(2)}$. *Orientational Order and Density.* Figure 1 shows $\langle P_2(\cos \theta^{(2)})\rangle$ as a function of $\mu_2^{(2)}$ for the four different chain lengths listed in Table 1. This plot shows that at small orientation potentials, the relationship between $\langle P_2(\cos \theta^{(2)})\rangle$ and $\mu_2^{(2)}$ is linear and independent of the chain length. At larger orientation potential, the orientation order parameter $\langle P_2(\cos \theta^{(2)})\rangle$ increases more sharply, an effect which becomes more pronounced for the longer chains. The differences in response for the different chain lengths can be traced to the lower fraction of chain ends in systems with longer chains. Chain ends tend to reduce the system density and to exhibit greater orientational freedom. Both of these effects necessitate a higher orientation potential to realize a given level of system orientation. Figure 2 shows the computed density for systems of different chain length and increasing orientation. The isotropic densities are consistent with the values calculated from the polyethylene equation of state developed by von Meerwall et al.[40] Just as with the orientation, the density behavior changes qualitatively around $\mu_2^{(2)} = 0.15\ kT$: for $\mu_2^{(2)} < 0.15\ kT$, the density is roughly constant, while for $\mu_2^{(2)} > 0.15\ kT$, it increases dramatically. This upturn occurs at a normal stress difference of 15−20 MPa. As shown in the conformation analyses to follow, the two regions suggested by Figures 1 and 2 correspond to rotation of the *principal axes* of the molecule at low potential, followed by deformation of the molecule and an increase in the number of trans torsions at high potential. The latter allows for densification as chains become aligned.

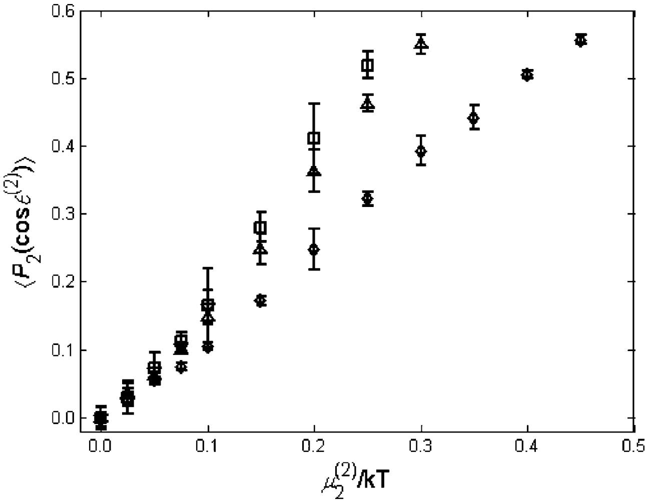

Figure 1. $\langle P_2(\cos \theta^{(2)})\rangle$ of polymer chains as a function of orientation potential for C_{24} (◇), C_{78} (△),C_{156} (□), C_{400} (▽).

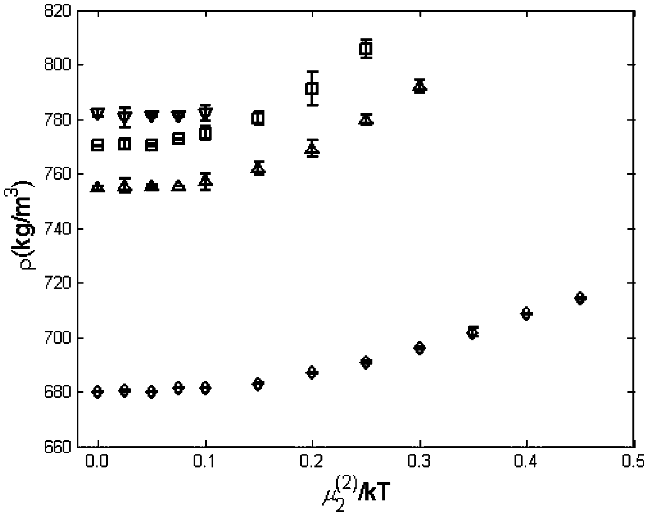

Figure 2. System density as a function of orientation potential for C_{24} (◇), C_{78} (△),C_{156} (□), C_{400} (▽).

Molecular Conformation. For each individual chain, the radius of gyration tensor is determined from the outer product of the individual intramolecular connector vectors:

$$\mathbf{R}_{g,j}^2 = n_j^{-2} \sum_{i=1}^{n_j-1} \sum_{i'>i}^{n_j} \mathbf{q}^{(i'-i)}\mathbf{q}^{(i'-i)} \tag{33}$$

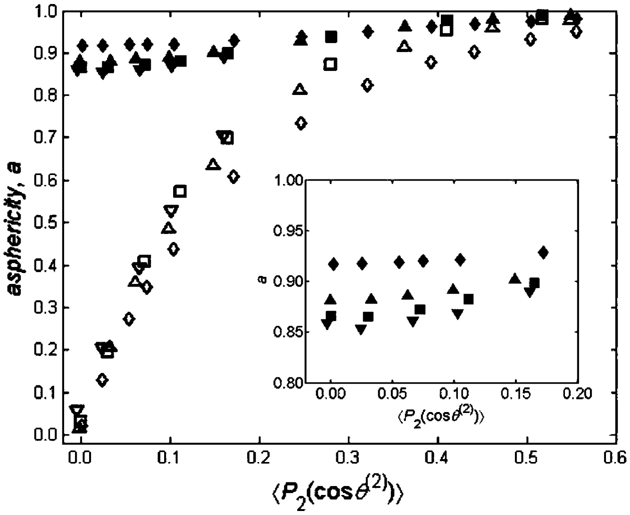

Figure 3. Molecular asphericity as a function of orientation order parameter $\langle P_2(\cos\theta^{(2)})\rangle$; laboratory reference for C_{24} (◇), C_{78} (△), C_{156} (□), C_{400} (▽); molecular reference for C_{24} (◆), C_{78} (▲), C_{156} (■), C_{400} (▼). Inset: expanded view of molecular asphericity for low-orientation order parameters.

The eigenvalues of this tensor define an ellipsoid that characterizes the size and shape of the molecule, while the eigenvectors define the principal axes and the molecular frame of reference. Averaging the radius of gyration tensor over all chains *j* and then obtaining the eigenvalues results in a system average molecular shape in the laboratory frame of reference, defined by the orientation potential. Alternatively, determining the eigenvalues molecule by molecule, sorting the eigenvalues for each molecule in decreasing order (i.e., $\lambda_1 > \lambda_2 > \lambda_3$), and then averaging each λ_i over all chains *j* results in a system-averaged molecular shape in the molecular frame of reference, defined by the principal axes of each molecule. The asphericity of the molecule is defined as:

$$a = 1 - \frac{\lambda_2^2 + \lambda_3^2}{2\lambda_1^2} \tag{34}$$

where the eigenvalues correspond to those averaged in either the laboratory or the molecular frame of reference. For an isotropic system, the asphericity in the laboratory frame is zero, while that in the molecular frame is significantly different from zero.[41]

As shown in Figure 3, the asphericity in the laboratory frame increases dramatically at low orientation potential, with little change in asphericity in the molecular frame. This is indicative of rotation of the principal axes of the molecules in response to the orientation potential, with little change in the size or shape of the molecules. At high orientation potential, the molecular asphericity increases, indicative of deformation and elongation of the molecules. The point at which this change in the behavior of the radius of gyration occurs is commensurate with the changes in density and local orientation order parameter $\langle P_2(\cos\theta^{(2)})\rangle$ mentioned previously.

Molecular size and shape are altered primarily through unraveling of the molecule via torsional rearrangement. The torsion angle distribution of the molecule thus provides another way to assess whether the orientation is occurring through rotation or deformation of the molecule. Figure 4 shows the fraction of torsions in the trans state as a function of increasing orientation potential, where torsion angles between $-\pi/3$ and $+\pi/3$ radians were considered to be in the trans state. For $\mu_2^{(2)} < 0.15\ kT$, the trans fraction is little changed; for $\mu_2^{(2)} > 0.15\ kT$, it increases, indicative of an unraveling of the chain.

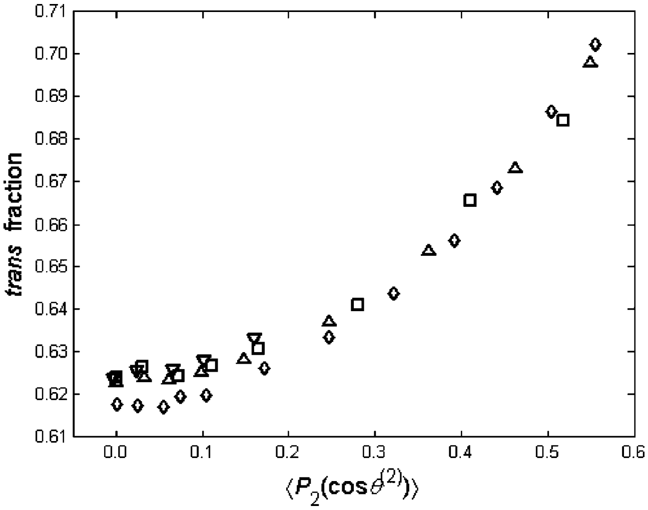

Figure 4. Fraction of trans bonds as a function of orientation order parameter $\langle P_2(\cos\theta^{(2)})\rangle$ for C_{24} (◇), C_{78} (△), C_{156} (□), C_{400} (▽).

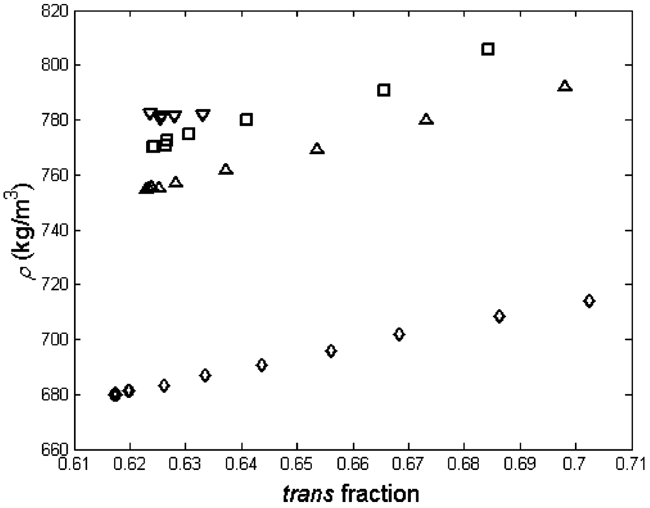

Figure 5. Density as a function of the fraction of trans bonds for C_{24} (◇), C_{78} (△), C_{156} (□), C_{400} (▽).

A comparison of Figures 2 and 4 reveals that a correlation exists between density and fraction of torsions in the trans state. This correlation is shown explicitly in Figure 5. It has been proposed that such a relationship could be responsible for the formation of a dense liquid phase in coexistence with a less dense liquid by spinodal decomposition due to spontaneous segregation of trans-rich regions from trans-poor regions in the melt.[42] Evidence in favor of this spinodal decomposition has been suggested based on small-angle X-ray diffraction data on polymer melts.[43,44] The length scale of density fluctuations is on the order of 10−100 nm, larger than the simulations performed here. Thus, the oriented melt phases produced by the SGMC simulation are representative volume elements of the dense liquid phase and can be used to estimate the free energy of such phases relative to that of the isotropic melt. A first-principles analysis of the spinodal decomposition mechanism is thus possible by this approach, but it is beyond the scope of the current work.

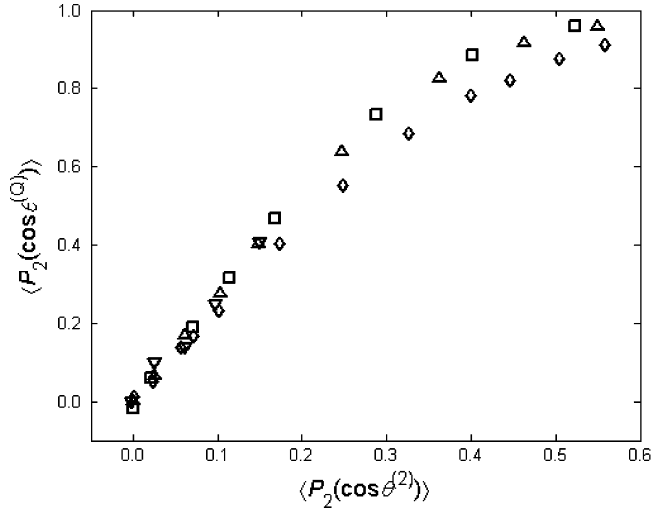

Figure 6. Molecular orientation order parameter vs local orientation order parameter for C_{24} (◇), C_{78} (△), C_{156} (□), C_{400} (▽).

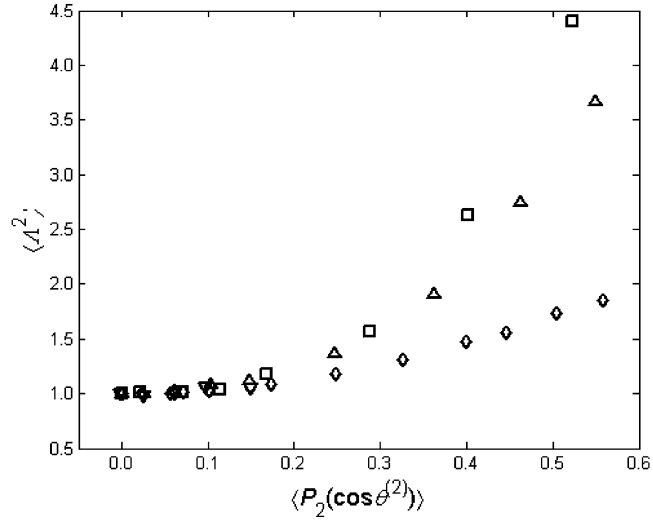

Figure 7. Molecular size as a function of local chain direction for C_{24} (◇), C_{78} (△), C_{156} (□), C_{400} (▽).

End-to-End Vector. We next consider the change in the end-to-end vector of the molecules as the orientation potential is applied for the systems described in Table 1. In Figure 6 and Figure 7, molecular orientation order parameter, $\langle P_2(\cos\theta^{(Q)})\rangle$, where $\theta^{(Q)}$ is the angle formed by the end-to-end vector of the molecule with the orientation axis, and molecular size, Λ^2, respectively, are plotted against the local orientation order parameter, $\langle P_2(\cos\theta^{(2)})\rangle$, to show the changes in orientation and size of the molecules. At low orientation, the molecular orientation order parameter is roughly proportional to the local orientation order parameter, while the molecular size is essentially unchanged; this regime corresponds to rotation of the principal axes of the molecules in the direction of orientation. Subsequent increases in $\langle P_2(\cos\theta^{(2)})\rangle$ produce relatively smaller changes in $\langle P_2(\cos\theta^{(Q)})\rangle$, but larger changes in $\langle\Lambda^2\rangle$, consistent with significant deformation of the polymer molecules. This effect is stronger for the longer chains.

B. The Stress-Optical Coefficient. Orientation plays a primary role in the development of birefringence. As the molecules orient, the difference in the optical properties along the chain and perpendicular to the chain produce an increasingly birefringent material. The empirical observation that the birefringence, Δn, is proportional to the normal stress difference $\Delta\tau = \tau_{xx} - \tau_{yy}$ at low $\Delta\tau$ is known as the stress-optical rule. The stress-optical coefficient is defined as:

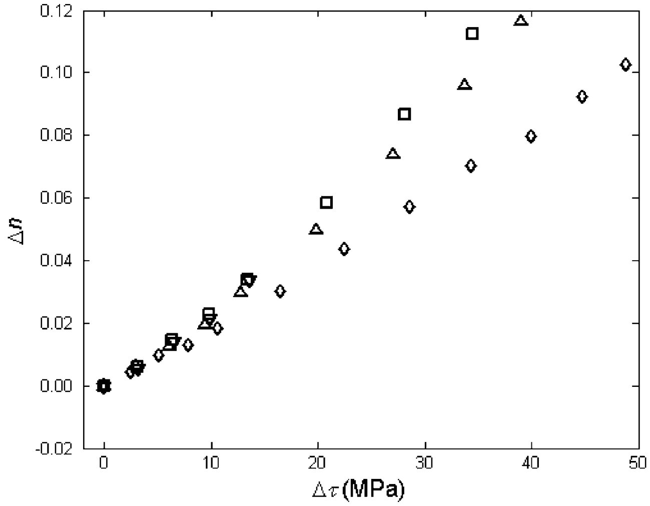

Figure 8. Birefringence as a function of normal stress difference for C_{24} (◇), C_{78} (△), C_{156} (□), C_{400} (▽).

$$C \equiv \frac{\Delta n}{\Delta\tau} \tag{35}$$

This proportionality holds true in regions without significant molecular deformation. The normal stress difference $\Delta\tau$ can be measured through the determination of the forces originating with the physical isomeric potential as shown in the Appendix, and the birefringence Δn is calculated as described by Mavrantzas and Theodorou:[31]

$$\Delta n = \frac{2}{9\pi}\frac{N}{V}\frac{(n^2+2)^2}{n}\left(\alpha_{11}^{(\mathrm{opt})} - \frac{\alpha_{22}^{(\mathrm{opt})} + \alpha_{33}^{(\mathrm{opt})}}{2}\right)\langle P_2(\cos\theta^{(2)})\rangle \tag{36}$$

The values of the diagonal elements of the optical polarizability tensor $\alpha^{(\mathrm{opt})}$ represent the principal components for a fully trans conformation of PE. The values, $\alpha_{11}^{(\mathrm{opt})} = 2.458$, $\alpha_{22}^{(\mathrm{opt})} = 1.903$, and $\alpha_{33}^{(\mathrm{opt})} = 1.458$, were obtained from Mavrantzas and Theodorou[31] and assume an equilibrium bond angle complement of 68°; N/V is the number density of polarizable species; The refractive index n of polyethylene is described by the following relation:[45]

$$\rho(g/cc) = 0.3276\,\frac{n^2-1}{n^2+2} \tag{37}$$

While the birefringence is most strongly affected by orientation, it is also dependent on density, as apparent from eqs 36 and 37.

From a series of simulations, Mavrantzas and Theordorou[31,32] calculated C for polyethylene to within 35% of its experimentally observed value. They attributed the error to the intrinsic stiffness of their intramolecular potential, but acknowledged that the observed length dependence of this quantity could indicate artifacts in the simulation due to the choice of state variable. The accurate calculation of C is significant in the current context because Δn depends primarily on the local chain direction and $\Delta\tau$ is sensitive to the manner in which the orientation potential is applied.

Reported experimental values of C for polyethylene melts are 2.0 GPa^{-1} (403 K)[46] and 2.2 GPa^{-1} (413 K).[47] Figure 8

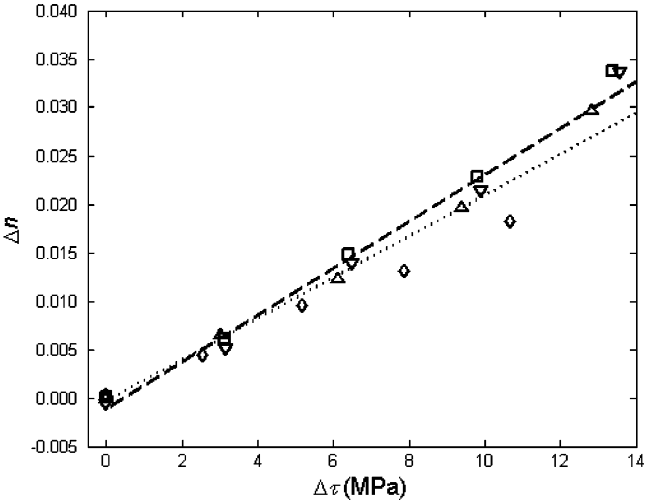

Figure 9. Birefringence as a function of normal stress difference for C_{24} (◇), C_{78} (△), C_{156} (□), C_{400} (▽). The lower line represents a fit of the data below $\Delta\tau = 7$ MPa; the upper line uses all of the points shown except for the C_{24} data above $\Delta\tau = 7$ MPa.

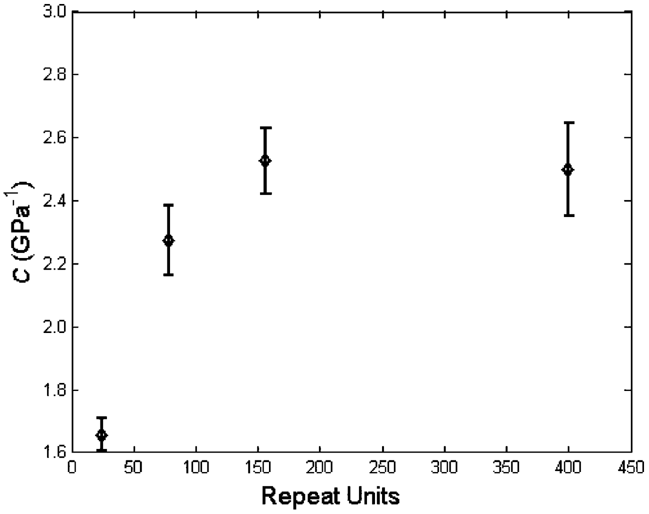

Figure 10. Stress-optical coefficient (C) as a function of number of repeat units; Each point is a regression of the data shown in Figure 9.

shows the plot of $\Delta\tau$ vs Δn, with an expanded view of the region at low $\Delta\tau$ shown in Figure 9. Figure 9 shows that the relationship is approximately linear for $\Delta\tau < 15$ MPa. At larger $\Delta\tau$, the relationship becomes nonlinear, co-incident with the crossover from molecular rotation to molecular deformation. Changes in birefringence due to density account for only about 5% of C for the highest orientations of C_{24}, C_{78}, and C_{156}.

Two linear regressions of the data are shown in Figure 9: The lower regression uses all of the points below 4 MPa and yields an estimate for the stress-optical coefficient C of 2.1 GPa^{-1}; the upper regression uses all of the points shown except the C_{24} points >7 MPa and yields a C of 2.4 GPa^{-1}. Both are in good agreement with the experimental data. One notable feature of these results is that they do not reproduce the large MW dependence seen by Mavrantzas and Theodorou[31,32] in which C exhibited a maximum for C_{78}, with a value almost 3 times that obtained for high-molecular-weight polyethylene. As shown in Figure 10, our results indicate that C approaches an asymptotic value of about 2.5 GPa^{-1} for high-molecular-weight polyethylene. The shape of this curve mirrors that of the simulated isotropic refractive index n, which also reaches its asymptotic value at a chain length of about 150 carbons.

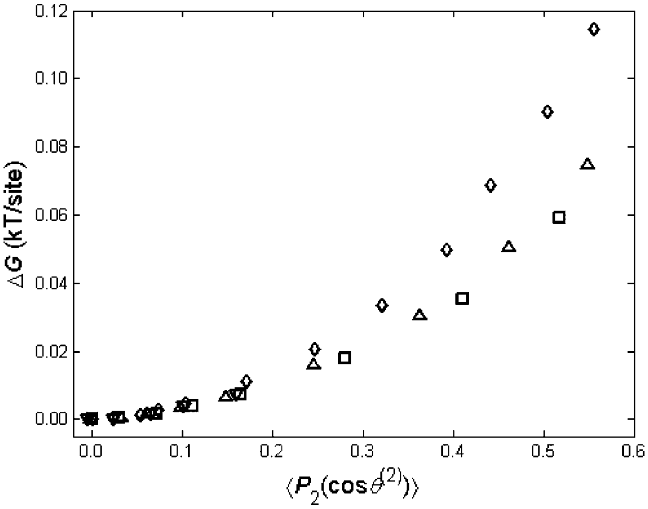

Figure 11. Free energy as a function of orientation order parameter for C_{24} (◇), C_{78} (△), C_{156} (□), C_{400}(▽).

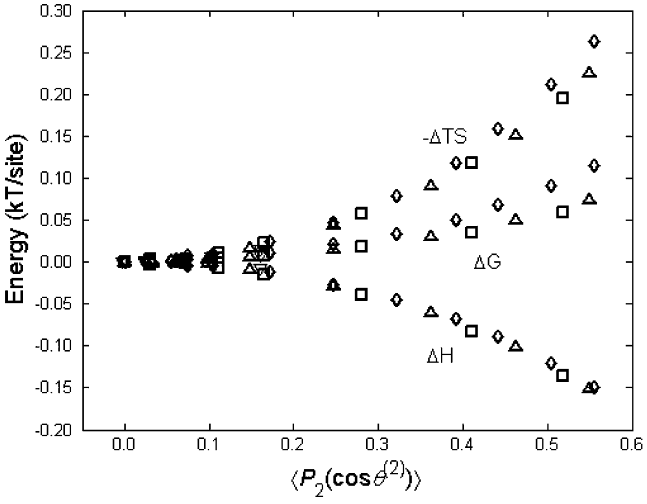

Figure 12. Contributions to the free energy as a function of orientation for C_{24} (◇), C_{78} (△), C_{156} (□), C_{400} (▽).

C. Work of Orientation. The SGMC method minimizes the free energy of the system simulated. A useful consequence of this is that one can obtain the reversible work of orientation through a thermodynamic integration with respect to the orientation potential μ. The work of orientation is taken with reference to the isotropic state at the same pressure and temperature. We computed the integral using the self-consistent histogram method.[17] Figure 11 shows that the work of orientation for the potential defined in eq 29 is molecular weight-dependent and that it requires less work to orient the longer chains. The ability to calculate the free energy allows us to determine the relative contributions of the loss of entropy and of the change in enthalpy, as shown in Figure 12. We observe that the enthalpic contribution to the work of orientation is comparable for all four molecular weights; the greater work required to orient the C_{24} chains is due to the larger entropy to be overcome for this low-molecular-weight system.

D. Simulations using the End-to-End Potentials, $\mu_2^{(S)}$ and $\mu_2^{(Q)}$. The results presented in the preceding section were generated exclusively through the application of a local orientation potential according to eq 29. Next, we discuss results from simulations using the potentials (eqs 31 and 32) acting on $\mathbf{Q}_j$. The potential described by eq 32 in particular reproduces simulations similar to those of refs 30−33 for the case of a

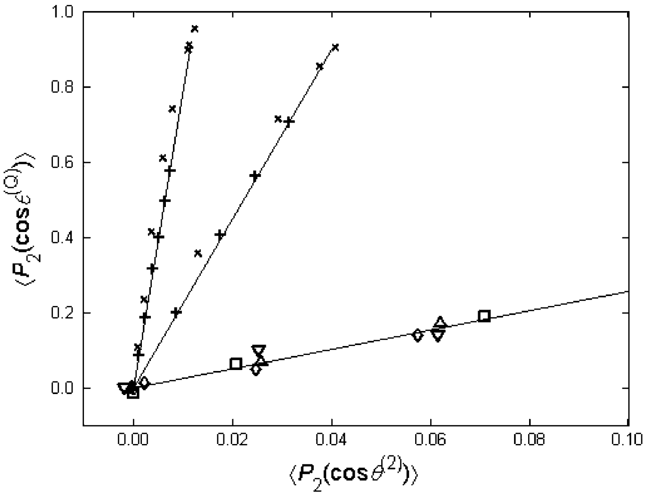

Figure 13. Molecular orientation order parameter as a function of local orientation order parameter. Application of the local potential $\mu_2^{(2)}$ for C_{24} (◇), C_{78} (△), C_{156} (□), C_{400} (▽); application of the end-to-end potential $\mu_2^{(S)}$ (+) and $\mu_2^{(Q)}$ (×) for C_{24} (intermediate line) and C_{78} (leftmost line). Lines are best-fit with slopes of 79, 22, and 2.5.

traceless α tensor and a single conformation tensor model. The traceless form of α is consistent with the kinematic interpretation presented in ref 33 for uniaxial elongational flow. Unfortunately, there are nontrivial differences in the polyethylene force field, in the applied potential, and in the measured quantities between the present work and those referenced: refs 30−32 use an α that is not traceless; ref 33 employs a traceless α, but applies it to a multiple conformation tensor model based on normal modes rather than as defined in refs 30−32 and in eq 18 here. Nevertheless, the response of the conformation tensor components $\langle c_{xx}\rangle$ and $\langle c_{yy}\rangle$ versus $\Delta\tau$ from the C_{78} simulations using eq 32 are in reasonable accord with the corresponding first normal modes plotted in Figure 1 of ref 33 (data not shown) and confirm the analogous behavior of the two approaches.

Of course, in the spirit of modeling experimental data, the SGMC approach presented here presupposes some knowledge about the chain conformation such as the conformation tensor predicted by rheological modeling. The melt elasticity approach presumes instead a kinematic interpretation of α in terms of velocity gradients.[33] Either way, the information provided to the simulation is molecular in nature rather than local, as was the case for birefringence measurements. Thus, it may produce a qualitatively different picture of the ordering of the molecule. One of the most striking demonstrations of this is the relationship between $\langle P_2(\cos\theta^{(2)})\rangle$ and $\langle P_2(\cos\theta^{(Q)})\rangle$ shown in Figure 13. Compared to Figure 6, the local orientation $\langle P_2(\cos\theta^{(2)})\rangle$ is much lower for the same $\langle P_2(\cos\theta^{(Q)})\rangle$ when the potential is applied to the end-to-end vectors. The two end-to-end potentials produce similar results even though one acts on both the orientation and size of the conformation tensor while the other acts only on the orientation of the principal axes of the conformation tensor. The proportionality between $\langle P_2(\cos\theta^{(Q)})\rangle$ and $\langle P_2(\cos\theta^{(2)})\rangle$ is molecular-weight-dependent for all values of the molecular orientation potentials $\mu_2^{(Q)}$ and $\mu_2^{(S)}$. This contrasts with the situation for $\mu_2^{(2)}$, which is molecular-weight independent for $\mu_2^{(2)} < 0.15$ kT. This can be explained by the nature of the potential in the two instances. For the end-to-end potential, if the entire chain is properly equilibrated, one expects additivity of the local orientation such that $\langle P_2(\cos\theta^{(2)})\rangle \approx \langle P_2(\cos\theta^{(Q)})\rangle/(n_j - 1)$ because of the long-range correlation. For a local orientation potential, the correlations along the chain contour and thus the persistence length are independent of chain length, provided the chains are of sufficient length. This is exactly what we observe; the best-fit slopes of the lines in Figure 13 are 79 and 22, in good agreement with $(\langle n_j\rangle - 1)$ for $\langle n_j\rangle = 78$ and 24, respectively. For the local orientation, the slope is about 2.5 and independent of chain size for low degrees of orientation.

5. Conclusions

We describe a general strategy for using Monte Carlo simulation in the semi-grand canonical ensemble to study nonequilibrium polymer systems. The method takes advantage of a generalized treatment of speciation of a system to encompass physical species as well as chemical species; the thermodynamics are otherwise unaltered. The physical speciation is then allowed to be polydisperse and the distribution transformed so that a more convenient set of species types is defined for the case of orientation. Assigning potentials to one or more members of the new list of physical species allows the method to be applied to a wide variety of experimental methods; it is sufficient that the measured property can be computed as an ensemble average of individual molecular conformations. We have shown how the local orientation, characterized through measurements of birefringence for example, can be used to infer information about the molecular shape, torsion distributions, and work of orientation. These results produce the most likely ensemble of structures by taking the least restrictive interpretation of the data.

For the specific case of polyethylene, our results confirm two qualitatively different mechanisms for orientation, also observed by Mavrantzas and Theodorou,[30] with a transition occurring at a normal stress difference of approximately 15−20 MPa for all molecular weights studied. Below this point, the molecular axes undergo rotation with little molecular deformation. We also observe a proportionality between the local and end-to-end orientation order parameters $\langle P_2(\cos\theta^{(2)})\rangle$ and $\langle P_2(\cos\theta^{(Q)})\rangle$ that is independent of the molecular weight. We estimate the stress-optical coefficient in good agreement with the literature values and find it to be relatively insensitive to molecular weight for C_{78} and higher. The most important factor that limits the range of applicability of the stress-optical rule is the degree to which orientation occurs primarily through molecular rotation; changes in the density account for a small part of the nonlinearity in the stress optical coefficient. At higher normal stress difference, the molecules experience significant deformation, as characterized by the trans fraction of torsions, the end-to-end vectors, and the asphericity of the molecules.

We also show that different results are obtained depending on whether the orientation is applied locally, to bond segments, or at the molecular level, to the end-to-end vector. The latter is well described by the additivity of the local order parameter. Studies probing oriented polyethylene melts simultaneously at different length scales would provide guidance as to which of these physical potentials is more relevant. Bent and co-workers[48] have performed simultaneous birefringence and SANS measurements of nonequilibrium polystyrene melts. However, such experiments are currently lacking for polyethylene, to the best of our knowledge.

Acknowledgment. This work was supported by the Center for Advanced Engineering Fibers and Films (CAEFF) of the Engineering Research Centers Program of the National Science Foundation, under NSF award no. EEC-9731680.

Appendix

We demonstrate the calculation of the virial stress contributions of the terms containing $\mu_2^{(Q)}$ (eq 25) and $\mu_2^{(S)}$ (eq 26) for

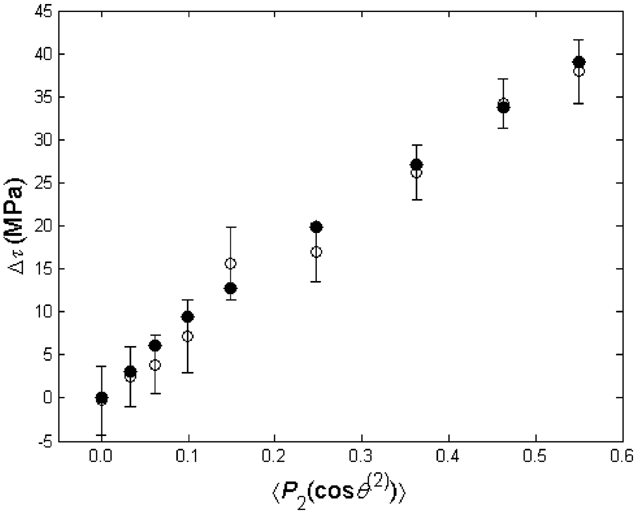

Figure 14. Open circles with error bars represent the normal stress difference measured using the molecular virial stress; the filled circles represent the normal stress difference calculated from eq A4.

which the end-to-end vector is $\mathbf{Q}_j$. The results for the end-to-end connector can be generalized to other connector vectors.

Contribution of $\mu_2^{(S)}$. We are concerned only with the diagonal components of the virial tensor because: (1) off-diagonal components are *on average* zero, and (2) only the diagonal components contribute to the pressure and to the normal stress difference. Thus, only one subscript is used to specify the component of the tensors $\mu_2^{(S)}$ and $\mu_2^{(Q)}$, and the subscript "2" is dropped to simplify notation. The trace of the virial stress due to the applied physical potential $\mu^{(S)}$ for an individual end-to-end vector (or connector vector) is calculated as:

$$tr(\mathbf{W}^{(\mu)}) = \sum_i W_{ii}^{(\mu)} = \sum_i Q_i \frac{\partial}{\partial Q_i} \mu^{(S)}{:}\mathbf{S} = \sum_i Q_i \frac{\partial \sum_j \mu_j^{(S)} P_2(Q_j)}{\partial Q_i} \qquad \text{(A1)}$$

where i and j both index Cartesian coordinates. Performing the partial differentiation for $P_2(Q_j) = {}^1/_2(3Q_j^2/|\mathbf{Q}^2| - 1)$, eq A1 becomes:

$$tr(\mathbf{W}^{(\mu)}) = 3 \sum_i \left(\mu_i^{(S)} \frac{Q_i^{\ 2}}{|\mathbf{Q}^2|} - \frac{Q_i^{\ 2}}{|\mathbf{Q}^2|} \sum_j \mu_j^{(S)} \frac{Q_j^{\ 2}}{|\mathbf{Q}^2|} \right) = 3 \left(\sum_i \mu_i^{(S)} \frac{Q_i^{\ 2}}{|\mathbf{Q}^2|} - \sum_j \mu_j^{(S)} \frac{Q_j^{\ 2}}{|\mathbf{Q}^2|} \right) = 0 \qquad \text{(A2)}$$

Equation A2 shows that there is no change in the pressure of the system due to the application of an arbitrary $\{\mu_i^{(S)}\}$.

Defining $M_i = \mu_i^{(S)} Q_i^2/|\mathbf{Q}^2|$ and taking the sum over the N_μ interactions in the system volume V, the normal stress difference for a uniaxial potential is seen to be:

$$\Delta\tau^{(\mu)} = \frac{N_\mu \langle W_{xx}^{(\mu)} - W_{yy}^{(\mu)} \rangle}{V} = \frac{N_\mu}{V} \left\langle M_x - M_y + \frac{Q_y^2 - Q_x^2}{|\mathbf{Q}^2|} \sum_j M_j \right\rangle \qquad \text{(A3)}$$

Contribution of $\mu_2^{(Q)}$. Similarly, the trace of the virial stress due to the applied physical potential $\mu^{(Q)}$ for an individual end-to-end vector (or connector vector) can be calculated:

$$tr(\mathbf{W}^{(\mu)}) = \sum_i W_{ii}^{(\mu)} = \sum_i Q_i \frac{\partial}{\partial Q_i} \Lambda^2 \mu^{(Q)}{:}\mathbf{S} = \frac{1}{2\langle|\mathbf{Q}^2|\rangle_0} \sum_i Q_i \frac{\partial \sum_j \mu_j^{(Q)} (3Q_j^{\ 2} - |\mathbf{Q}^2|)}{\partial Q_i} \qquad \text{(A4)}$$

Partial differentiation obtains the following expression for the pressure contribution:

$$tr(\mathbf{W}^{(\mu)}) = \frac{1}{\langle|\mathbf{Q}^2|\rangle_0} \sum_i Q_i^2 (3\mu_i^{(Q)} - \sum_j \mu_j^{(Q)}) \qquad \text{(A5)}$$

If we consider a traceless form of μ (= 2α), the final result is:

$$tr(\mathbf{W}^{(\mu)}) = \frac{3 \sum_i \mu_i^{(Q)} Q_i^2}{\langle|\mathbf{Q}^2|\rangle_0} \neq 0 \qquad \text{(A6)}$$

The contribution to the pressure will therefore be:

$$\Delta P^{(\mu)} = \frac{N_\mu \langle tr(\mathbf{W}^{(\mu)}) \rangle}{V} = \frac{3N_\mu}{V} \left\langle \frac{\sum_i \mu_i^{(Q)} Q_i^2}{\langle|\mathbf{Q}^2|\rangle_0} \right\rangle \qquad \text{(A7)}$$

This accounts for the necessary introduction of a conjugate variable to the volume of $P = 3b + \Delta P^{(\mu)}$, where b is the conjugate thermodynamic variable to volume in the constant pressure simulations.

Comparison of Normal Stress Difference Using the Virial Equation and the Orientation Fluctuations. Equation A3 can be used to calculate the normal stress difference from a local physical isomer potential by replacing N_μ with the number of interactions $N - 2N_{\mathrm{ch}}$ and $\mathbf{Q}$ with $\mathbf{q}^{(2)}$. Alternatively, one could obtain this quantity from the average virial stresses. However, the use of eq A3 is more accurate. Figure 14 shows a comparison of the two methods for calculating the normal stress differences for the series of simulations on C_{78} chains using a local isomer potential $\mu_2^{(2)}$. The error bars are only shown for the normal virial stress differences for clarity; the error bars on the normal stress differences calculated using eq A4 are one-half, or less, the size of the error bars on the virial. This shows the consistency of this approach with the simulation results.

References and Notes

(1) Rutledge, G. C. *Phys. Rev. E* **2001**, *63*, 021111.
(2) Schmidt-Rohr, K.; Hehn, M.; Schaeffer, D.; Spiess, H. W. *J. Chem. Phys.* **1992**, *97*, 2247.
(3) Lewis, R. H.; Long, H. W.; Schmidt-Rohr, K.; Speiss, H. W. *J. Magn. Res., Ser. A* **1995**, *115*, 26.
(4) Robyr, P.; Meier, B. H.; Ernst, R. R. *Chem. Phys. Lett.* **1991**, *187*, 471.
(5) Liao, M. Y.; Rutledge, G. C. *Macromolecules* **1997**, *30*, 7546.
(6) *Structure and Properties of Oriented Polymers*; Ward, I. M., Ed.; Chapman and Hall: London 1997.

(7) Martyushev, L. M.; Seleznev, V. D. *Phys. Rep.* **2006**, *426*, 1.
(8) McGreevy, R. L. *J. Phys.: Condens. Matter* **2001**, *13*, R877.
(9) Fouda, I. M.; Shabana, H. M. *Polym. Int.* **1999**, *48*, 181.
(10) Mabrouk, M. A.; Shams-Eldin, M. A. *Pure Appl. Opt.* **1996**, *5*, 929.
(11) Shan, H.; White, J. L. *J. Appl. Polym. Sci.* **2004**, *93* 9.
(12) Ko, M. J.; Waheed, N.; Lavine, M. S.; Rutledge, G. C. *J. Chem. Phys.* **2004**, *121*, 2823.
(13) Koyama, A.; Yamamoto, T.; Fukao, K.; Miyamoto, Y. *J. Macromol. Sci. Phys.* **2003**, *B42*, 821.
(14) Briano, J. G.; Glandt, E. D. *J. Chem. Phys.* **1984**, *80*, 3336.
(15) Bathe, M.; Rutledge, G. C. *J. Comput. Chem.* **2003**, *24*, 876.
(16) Wilding, N. B. *J. Chem. Phys.* **2003**, *119*, 12163.
(17) Ferrenberg, A. M.; Swendsen, R. H. *Phys. Rev. Lett.* **1989**, *63*, 1195.
(18) Gō, N. *Annu. Rev. Biophys. Bioeng.* **1983**, *12*, 183.
(19) Soper, A. K. *Chem. Phys.* **1996**, *202*, 295.
(20) Lyubartsev, A. P.; Laaksonen, A. *Phys. Rev. E* **1995**, *52*, 3730.
(21) Meyer, H.; Biermann, R.; Faller, R.; Reith, D.; Muller-Plathe, F. *J. Chem. Phys.* **2000**, *113*, 6264.
(22) Jain, S.; Garde, S.; Kumar, S. K. *Ind. Eng. Chem. Res.* **2006**, *45*, 5614.
(23) Colhoun, F. L.; Armstrong, R. C.; Rutledge, G. C. *Macromolecules* **2002**, *35*, 6032.
(24) Jaynes, E. T. *Phys. Rev.* **1957**, *106*, 620.
(25) van Gurp, M. *J. Rheol.* **1998**, *42*, 1269.
(26) Tagliani, A. *J. Math. Phys.* **1993**, *34*, 326.
(27) Mead, L. R.; Papanicolaou, N. *J. Math. Phys.* **1984**, *25*, 2404.
(28) Guiasu, S. *Information Theory with Applications*; McGraw-Hill: New York, 1977, Chapter 4.
(29) Agmon, N.; Alhassid, Y.; Levine, R. D. *J. Comput. Phys.* **1979**, *30*, 250.
(30) Mavrantzas, V. G.; Theodorou, D. N. *Macromolecules* **1998**, *31*, 6310.
(31) Mavrantzas, V. G.; Theodorou, D. N. *Comput. Theor. Polym. Sci.* **2000**, *10*, 1.
(32) Mavrantzas, V. G.; Theodorou, D. N. *Macromol. Theor. Simul.* **2000**, *9*, 500.
(33) Mavrantzas, V. G.; Ottinger, H. C. *Macromolecules* **2002**, *35*, 960.
(34) Ottinger, H. C. *Rheol. Acta* **2001**, *40*, 317.
(35) Paul, W.; Yoon, D. Y.; Smith, G. D. *J. Chem. Phys.* **1995**, *103*, 1702.
(36) in't Veld, P. J.; Hutter, M.; Rutledge, G. C. *Macromolecules* **2006**, *39*, 439.
(37) Dodd, L. R.; Boone, T. D.; Theodorou, D. N. *Mol. Phys.* **1993**, *78*, 961.
(38) Pant, P. V. K.; Theodorou, D. N. *Macromolecules* **1995**, *28*, 7224.
(39) Mavrantzas, V. G.; Boone, T. D.; Zervopoulou, E.; Theodorou, D. N. *Macromolecules* **1999**, *32*, 5072.
(40) von Meerwall, E.; Beckman, S.; Jang, J.; Mattice, W. L. *J. Chem Phys.* **1998,** 108, 4299.
(41) Solc, K. *J. Chem Phys.* **1971**, *55*, 335.
(42) Olmstead, P. D.; Poon, W. C. K.; McLeish, T. C. B.; Terrill, N. J.; Ryan, A. J. *Phys. Rev. Lett.* **1998**, *81*, 373.
(43) Imai, M.; Kaji, K. *Polymer* **2006**, *47*, 5544.
(44) Ryan, A. J.; Fairclough, J. P. A.; Terrill, N. J.; Olmstead, P. D.; Poon, W. C. K. *Faraday Discuss.* **1999**, *112*, 13.
(45) Krishnaswamy, R. K.; Janzen, J. *Polym. Test.* **2005**, *24*, 762.
(46) Saunders, D. W. *Trans. Faraday Soc.* **1956**, *52*, 1425.
(47) Janeschitz-Kriegl, H. *Polymer Melt Rheology and Flow Birefringence*; Springer-Verlag: Berlin, 1983.
(48) Bent, J. F.; Richards, R. W.; Gough, T. D. *Rev. Sci. Instrum.* **2003**, *74*, 4052.

MA062935R